Development of a sustainable nitrogen-doped biochar desulfurizer for solid oxide fuel cell systems

Hendrik Setiawan[a*], Mio Sakamoto[b], Takaya Fujisaki[c], Stephen Matthew Lyth[b], and Yusuke Shiratori[b,d]

[a]Department of Hydrogen Energy Systems, Graduate School of Engineering, Kyushu University, 744 Motooka, Nishi-ku, Fukuoka 819-0395, Japan
[b]International Research Center for Hydrogen Energy, Kyushu University, 744 Motooka, Nishi-ku, Fukuoka 819-0395, Japan
[c]Institute of Multidisciplinary Research for Advanced Materials, Tohoku University, 2-1-1 Katahira, Aoba-ku, Sendai 980-8577, Japan
[d]Department of Mechanical Engineering, Faculty of Engineering, Kyushu University, 744 Motooka, Nishi-ku, Fukuoka 819-0395, Japan

**Corresponding author*: hendrik.swn@gmail.com

Solid oxide fuel cells (SOFCs) running on biogas can undergo performance degradation in the presence of trace H_2S. Here, a nitrogen-doped rice husk biochar was employed as a sustainable material for desulfurization via adsorption. Nitrogen-doping on the surface of the biochar was found to significantly promote H_2S adsorption. Biochar doped with nitrogen using NH_3 evaporated from ammonia solution exhibited 2.3 times higher total H_2S adsorption capacity compared to that treated with NH_3 gas. This was attributed to lower pyridinic-N content and in turn, suppressed O* formation, leading to better micropore utilization. The mass of nitrogen-doped biochar required for 100,000 h operation of a 1 kW SOFC was estimated to be 45 kg, indicating the clear viability of using sustainable materials for desulfurization of fuel streams.

Keywords: Biochar, H_2S, adsorption, digestate liquid, nitrogen-doping

This is a peer-reviewed, accepted author manuscript of the following article: Setiawan, H., Sakamoto, M., Fujisaki, T., Lyth, S. M., & Shiratori, Y. (2022). Development of a sustainable nitrogen-doped biochar desulfurizer for solid oxide fuel cell systems. Biomass and Bioenergy, 167, Article 106631. Advance online publication. https://doi.org/10.1016/j.biombioe.2022.106631

1. Introduction

Solid oxide fuel cells (SOFCs) using biogas are a promising technology for distributed power generation in e.g. the agricultural or food industries, with over double the efficiency of internal combustion engines [1]. The major components of biogas produced from agricultural waste are methane (CH_4, 45 to 75 vol%) and carbon dioxide (CO_2, 25 to 55 vol%) which are both major greenhouse gases, and the composition differs depending on feedstock and production site. Other minor constituents such as nitrogen (N_2, 0 to 5 vol%) and trace impurities such as hydrogen sulfide (H_2S, 500 to 3000 ppm) are also generally present [2,3]. It is well known that just several parts per million (ppm) of hydrogen sulfide in the fuel stream will deactivate the active sites for the steam methane reforming reaction (to produce H_2) and the hydrogen oxidation reaction (HOR) in SOFCs. Therefore, to achieve reasonable durability in a biogas-fueled SOFC the H_2S concentration should ideally be reduced to less than 1 ppm [4–6]. A two-step desulfurization process is generally employed, comprising (i) a chemical reaction with iron oxide, and (ii) physical adsorption. The iron oxide pellets used in the first desulfurization step are inexpensive and readily available even in rural areas. However, in the second step, a commercially available adsorbent such as zeolite or activated carbon is usually applied, which are more expensive and not as readily available [7]. A more affordable H_2S adsorbent produced from locally sourced materials would be a huge advantage, especially for SOFC deployment in developing economies. As such, this study focuses on biochar, a biomass-derived carbon which can be locally produced.

Biochar is an organic porous carbon material obtained by heat treatment of biomass such as agricultural waste, forestry waste, and livestock manure in O_2-free condition (pyrolysis) that has been widely used as a low cost adsorbent [8,9]. Utilization as a renewable fuel [10,11], and the application to agriculture as soil amendment to increase the nitrogen uptake and water retention abilities have also been reported [12–14]. Biochar materials rich in alkaline minerals or with reactive surface functional groups have previously been reported for the removal of heavy metals and acidic gases [15,16]. Depending on the source and treatment process, biochar can behave as a physical adsorbent (with adsorption capacity governed by surface area and porosity), and/or a chemical adsorbent (relying on reactions between the target molecule and the biochar surface) [17]. In the case of chemical adsorption, surface modification by alkali inclusions, metal loading, or nitrogen-doping can be key factors in enhancing the total H_2S adsorption capacity (q). [18,19]

Adsorption and decomposition of H_2S on the surface of carbon materials and subsequent conversion to sulfur can be expressed by following equations:

$$H_2S \rightarrow H^+ + HS^- \quad (1)$$
$$HS^- + O^* \rightarrow S + OH^- \quad (2)$$

Reactive oxygen radicals (i.e. O*) on the surface promote the chemical adsorption of H_2S by reacting with hydrosulfide ions (HS^-) to form sulfur [20].

Meanwhile, nitrogen-doping has been reported to be effective in promoting the selective oxidation of H_2S [21]. As such, nitrogen-doping of biochar may be an effective method to improve its adsorption properties. Heat treatment in ammonia (NH_3) gas is one of the most

common methods of doping carbon with nitrogen [22]. However, in rural areas or developing economies, the use of pure NH_3 gas is not a viable approach in terms of cost or availability.

Biogas is produced by fermentation of biowaste. During the fermentation process, a considerable amount of digestate liquid is generated, and subsequently used as a liquid fertilizer [23]. In fact, this digestate liquid contains significant concentrations of ammonia (NH_3, 0.15–0.7 wt%) with a composition depending on the type of biomass feedstock [24]. In a system designed and built by the authors and located in Vietnam, the digestate liquid is further concentrated to 10 wt% NH_3 via electrodialysis, using the green electricity generated by a biogas-fueled SOFC [25].

Here we propose that concentrated digestate liquid can be used as a convenient and sustainable source of NH_3 for nitrogen-doping of biochar, to improve its hydrogen sulfide adsorption properties. We produce biochar from rice husk and dope it with nitrogen by heat treatment in either pure NH_3 obtained from a gas cylinder, or after bubbling nitrogen through a simulated digestate solution of NH_3, and investigate the performance of the resulting materials in H_2S adsorption.

2. Experimental

2.1. Production and nitrogen-doping of biochar

Rice husk from Japonica rice (Oryza sativa subs. Japonica) was collected from the Itoshima area of Fukuoka prefecture in Japan. This was first dried at 100 °C for 24 h in air. Then, 3 g of dried rice husk was pyrolyzed at 500 °C under flowing nitrogen (50 mL min^{-1}) for 120 min, to produce rice husk biochar (**RHBC**). Nitrogen-doping of RHBC was performed using two different methods. In the first method, 2 g of RHBC was heat treated for 120 minutes at 900°C in flowing NH_3 and N_2 (25:75 vol.%) with a total flow rate of 100 mL min^{-1} (Fig. 1a). This sample is labelled **RHBC-N1**. In the second method, an NH_3 solution was prepared with a concentration of 10 wt% to simulate concentrated digestate liquid. Carrier gas (N_2) was bubbled through this solution at 100 mL min^{-1} at 30°C (Fig. 1b), and the resulting gas flow is calculated to have an NH_3 content of 15.7 vol% and a water content of 3.8 vol%. Then, 2 g of RHBC was heated treated in this NH_3-rich gas at 850°C for 270 min. This sample is labelled **RHBC-N2**.

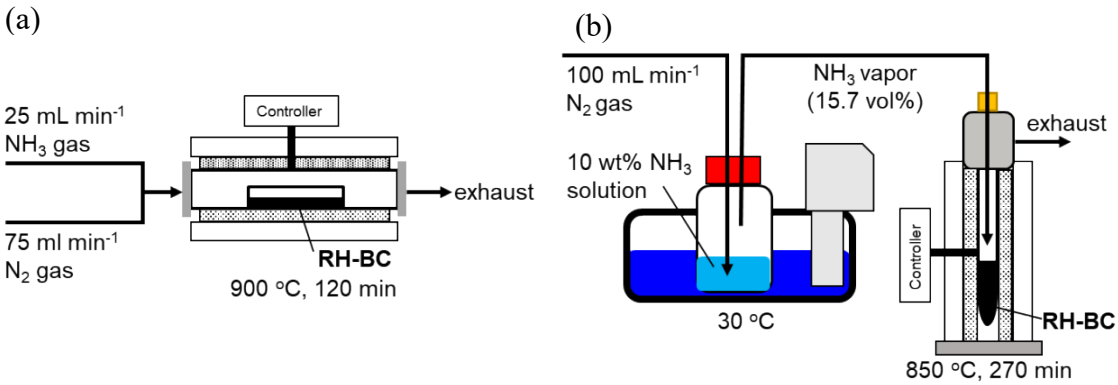

Figure 1. Schematic illustration of different methods to dope rice husk biochar with nitrogen: (a) using NH_3 gas from a cylinder, or (b) using N_2 gas bubbled through a 10 wt% ammonium solution, simulating digestate liquid.

2.2. Sample characterization

The volatile and non-volatile (i.e. ash) solids contents of the biochar samples, corresponding to organic and inorganic substances, respectively, were analyzed by thermogravimetry and differential thermal analysis (TG-DTA, Thermoplus EVO2, Rigaku Co., Ltd., Japan). A 10 mg sample was heated to 800°C at a rate of 10°C min^{-1} in 20 mL min^{-1} air flow and maintained at this temperature for 120 min, during which the weight loss and amount of residue were analyzed. Elemental analysis was performed using energy dispersive X-ray fluorescence analysis (XRF; EDX-7000, Shimadzu, Japan). For near-surface analysis, quasi-surface-sensitive technique using X-ray photoelectron spectroscopy (XPS) was done at room temperature using a monochromated Al Kα ($h\nu$ = 1,486.7 eV) X-ray source operated at 5 mA and 15 kV (Kratos Axis Ultra, Shimadzu, Japan). All binding energies (BEs) were normalized to the C1s line at 284.6 eV.

The specific surface area (SSA) was measured via the nitrogen adsorption method (Belsorp-mini II analyzer, MicrotracBEL Corp., Japan), and the pore size distribution was

evaluated via the MP micropore analysis method and the Barrett-Joiner-Halenda (BJH) method. The crystal structure was analyzed by X-ray diffractometry (XRD; Rint-Ultima III, Rigaku, Japan) with CuKα radiation at 40 kV and 40 mA in the 2θ range from 10° to 90° at 0.4° min^{-1}. Microstructure was investigated by field emission scanning electron microscopy (FESEM; S5200, Hitachi High-Technologies Corp., Japan) by energy dispersive X-ray spectroscopy (EDX) and scanning transmission electron microscopy (STEM; HD2300A, Hitachi High-Technologies).

2.3. Hydrogen sulfide adsorption test

The apparatus for measuring H_2S adsorption was designed as shown in Fig. 2. The biochar sample was packed into a glass fixed-bed reactor tube with an inner diameter of 0.75 cm, which was used as the adsorbent vessel. In every test, 1.0 g of powdered sample was packed into the tube.

The tests were conducted at room temperature by flowing nitrogen gas containing 40 ppm H_2S at 50 mL min^{-1} through the adsorbent vessel. The outlet gas was collected every 15 min in a 2,000 mL gas bag (F2S sampling bag, Asone Co.), and the H_2S concentration was monitored using a gas analyzer (Biogas 5000, Geotechnical Instrument Ltd., UK).

Breakthrough is defined as the point at which the adsorbate starts to penetrate the column and 1 ppm of adsorbate (the lower detection limit of Biogas 5000) is detected in the column effluent. After breakthrough was reached, the gas was collected every 120 min in a 2,000 mL plastic gas bag. The H_2S concentration was analyzed using two types of detector tubes with different measuring ranges of 1 to 40 ppm (4LK) and 0.25 to 120 ppm (4LL) (hydrogen sulfide detector tubes, Gastec Corporation, Japan). A one-to-one relation between the values of H_2S concentration measured by the analyzer and the detector tube were confirmed, confirming the reliability of the measurement.

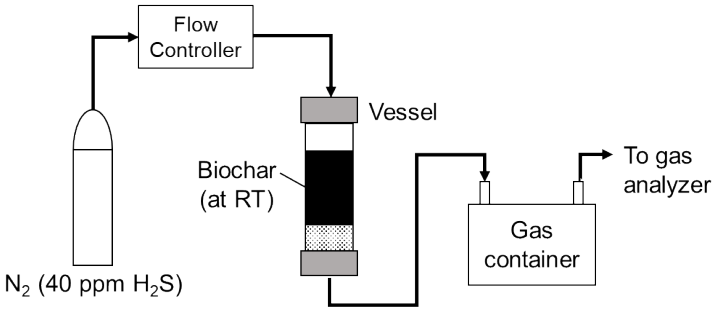

Figure 2. Apparatus used to evaluate the H_2S adsorption capacity of different biochars.

Adsorption curve to be measured is schematically shown in Fig. 3. The total H_2S adsorption capacity per gram of biochar (q), corresponds to the area above the adsorption curve, was calculated using the following equation:

$$q = (\rho v/m)\int_0^t (C_0 - C)dt \quad (3)$$

where ρ is the density of H_2S gas, v is the volumetric flow rate, m is the adsorbent (biochar) mass, C_0 is the H_2S concentration at the inlet, and C is the H_2S concentration at the outlet at time t.

q is the amount of H_2S adsorbed in a sample until the H_2S concentration in the outlet gas reaches 40 ppm. Meanwhile, the breakthrough adsorption capacity (q_o), corresponding to the surface affinity with H_2S, was estimated from the area indicated by lateral stripes of Fig. 3. The calculation was performed via trapezoidal rule approximation in MATLAB ver. R2019b (The Mathwork Inc., USA).

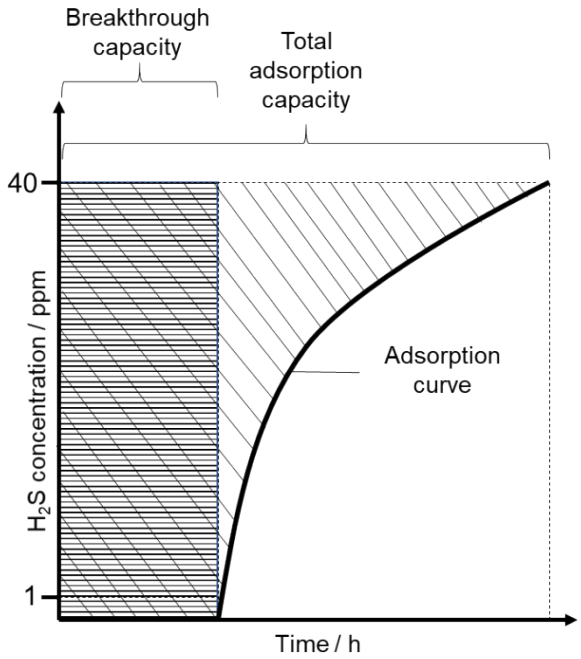

Figure 3. Example of an adsorption curve.

2.4. DFT calculation

Density functional theory (DFT) calculations were performed using the Vienna ab initio simulation package (VASP) [26–28]. The Perdew-Burke-Ernzerhof (PBE) [29] exchange-correlation functional was employed based on the projector-augmented wave (PAW) method [28]. The cutoff energy of the plane wave basis was set to 400 eV following previous study [30]. Firstly, 4 x 4 graphene sheet was constructed and optimized using 5 x 5 x 1 Monkhorst-Pack k-points mesh. Also, the spin polarization was considered. Pseudopotentials with valence states of C ($2s^2$, $2p^2$), N ($2s^2$, $2p^3$), S ($3s^2$, $3p^4$), O ($2s^2$, $2p^4$), and H (1s) were used in the calculations. All ionic positions were optimized by a conjugate gradient method until the forces on each ion were below 10^{-2} eV/Å. Electronic energy was converged to 10^{-6} eV. The graphene structurally optimized by the above process showed 1.426 Å as a length of C-C bond, which was in good agreement with previous results [31–33]. Then, N-doped structures containing pyridinic-, pyrrolic-, or graphitic-N were made in the graphene sheet. To calculate the van der Waals (vdW) interaction between the graphene sheet and oxygen molecule (O_2), Tkatchenko-Scheffler method was applied [30,34]. To discuss the stability of O_2 on pyridinic-N, pyrrolic-N, or graphitic-N, the interaction energy (E_{int}) was estimated for each N-doped site. E_{int} for the pyridinic-N can be expressed as follows,

$$E_{\mathrm{int}} = E_{\mathrm{O_2 + pyridinic-N}} - (E_{\mathrm{pyridinic-N}} + E_{\mathrm{O_2}}) \quad (4)$$

where $E_{O_2 + \text{ pyridinic} - N}$, $E_{\text{pyridinic} - N}$, and E_{O_2} are the electrostatic potentials of pyridinic-N with adsorbed O_2, pyridinic-N, and O_2, respectively [35]. The negative value of the interaction energy indicates that O_2 can adsorb on the pyridinic-N [36].

3. Results and discussion

3.1. Microstructure and elemental analysis

According to XRD of the as-prepared RH-BC sample, only a wide peak at around 2θ = 22° is detected (not shown). This is assigned to amorphous carbon (JCPDS card No. 22-1069). After the carbon was burned off, only the diffraction pattern of SiO_2 (JCPDS card No. 39-1425) was detected suggesting that SiO_2 was initially encapsulated by carbon [37]. The volatile solids content of the as-prepared RHBC was determined via TG-DTA to be 52.9 wt%, whilst the ash content was 47.1 wt%. The ash comprised 87.0 wt% SiO_2; 11.0 wt% K_2O; 0.98 wt% CaO; and 0.16 wt% Fe_2O_3, as measured by XRF. Previous research has shown that SiO_2, one of the major components of RHBC, has almost no adsorption capability, thus the treatment of RHBC should be performed so that the SiO_2 exposing to the surface can be suppressed [38]. Existence of the alkali oxides (K_2O and CaO) can help the adsorption of acid gases such as H_2S, however their effect is not discussed in this study, because the main adsorption site is the carbon surface doped with nitrogen [39].

FESEM-EDX images of RHBC are shown in Fig. 4. RHBC has a honeycomb-like pore structure (Fig. 4a), which is expected to have a low pressure-drop in a gas flow, however the gas mixing may be poor inside the tubular macropores. The honeycomb structure of the biochar originates from the carbonization of xylem and phloem vessels of plant, which act as water and nutrient transport pathways in the original plant [40]. The magnified image (Fig. 4b) shows the existence of smaller pores on the wall of the porous body (Fig. 4b) [41,42]. In the EDX mapping, only carbon was detected, showing that SiO_2 is covered by carbon (Figs. 4c and d).

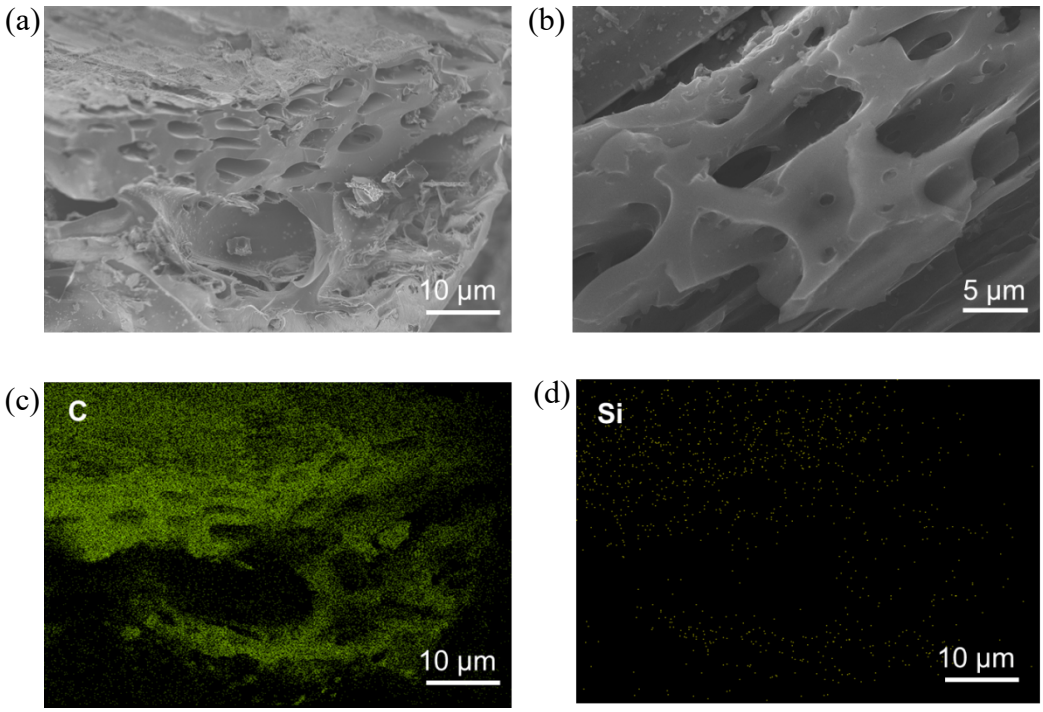

Figure 4. FESEM-EDX images of (a) RHBC and (b) the surface of the porous body of RHBC with the EDX mapping images of (c) C and (d) Si, respectively, for the FESEM image of (a).

The SSA of the prepared biochar samples are summarized in Table I, as measured by nitrogen adsorption. The SSA of the as-prepared RHBC was 146 m^2 g^{-1}. After NH_3 treatment (RHBC-N1) the total pore volume (V_{tot}) and the micropore volume (V_{mic}) increased significantly resulting in an increase in SSA. This increase is caused by the defect formation on the carbon surface as a result of the partial gasification (NH_3 etching) [38,43]. After NH_3 treatment using the simulated digestate liquid (RHBC-N2) the SSA and porosity did not significantly change compared to as-prepared RH-BC, because the NH_3 vapor (15.7% NH_3) in N2 treatment was unable to change the carbon structure as drastic as N1 treatment with 25% NH_3 gas.

The nitrogen (N) contents near the surface are also summarized in Table I, as measured by XPS. N was not detected near the surface of the pristine RHBC. After NH_3 treatment (RHBC-N1), this increased to 3.69 wt%, confirming that NH_3 treatment is a suitable method for nitrogen-doping. Using the simulated digestate liquid (RHBC-N2) results in a nitrogen content of 2.52 wt%. Nitrogen-doping has been shown to produce nitrogen functional groups on the surface by substituting oxygen bound on the carbon surface [22]. The decreases in the surface O from 19.2% to 15.7% and 16.9% for N1 and N2 treatments, respectively, indicate this substitution. The lower surface O content of RHBC-N1 compared to RHBC-N2 suggests the higher degree of nitrogen-doping of the N1 treatment.

TABLE I. Results of the BET measurements and the XPS quantification of the near-surface element of RHBC samples.

Sample	SSA / m^2 g^{-1}	V_{tot} / 10^{-7} m^3 g^{-1}	V_{mic} / 10^{-7} m^3 g^{-1}	Near-surface N / wt%	Near-surface O / wt%	Pyridinic-N content / wt%
RHBC	146	1.02	0.63	-	19.2	-
RHBC-N1	354	1.78	1.43	3.69	15.7	2.29
RHBC-N2	170	1.02	0.68	2.52	16.9	1.31

The XPS N 1s spectra for the biochar samples are summarized in Fig. 5, and deconvoluted into contributions from pyridinic-, pyrrolic-, and graphitic-N nitrogen sites, as illustrated in Fig. 5 [44,45]. The high temperature NH_3 treatment produces thermally stable nitrogen groups, pyridinic-, pyrrolic-, and graphitic-N with pyridinic-N as dominant [17,46]. RHBC-N1 has much higher pyridinic content (2.29 wt%) than RHBC-N2 (1.31 wt%) due to higher concentration of NH_3 and slightly higher treatment temperature. The higher pyridinic-N content will make the surface of RHBC-N1 more active for chemically adsorbing H_2S.

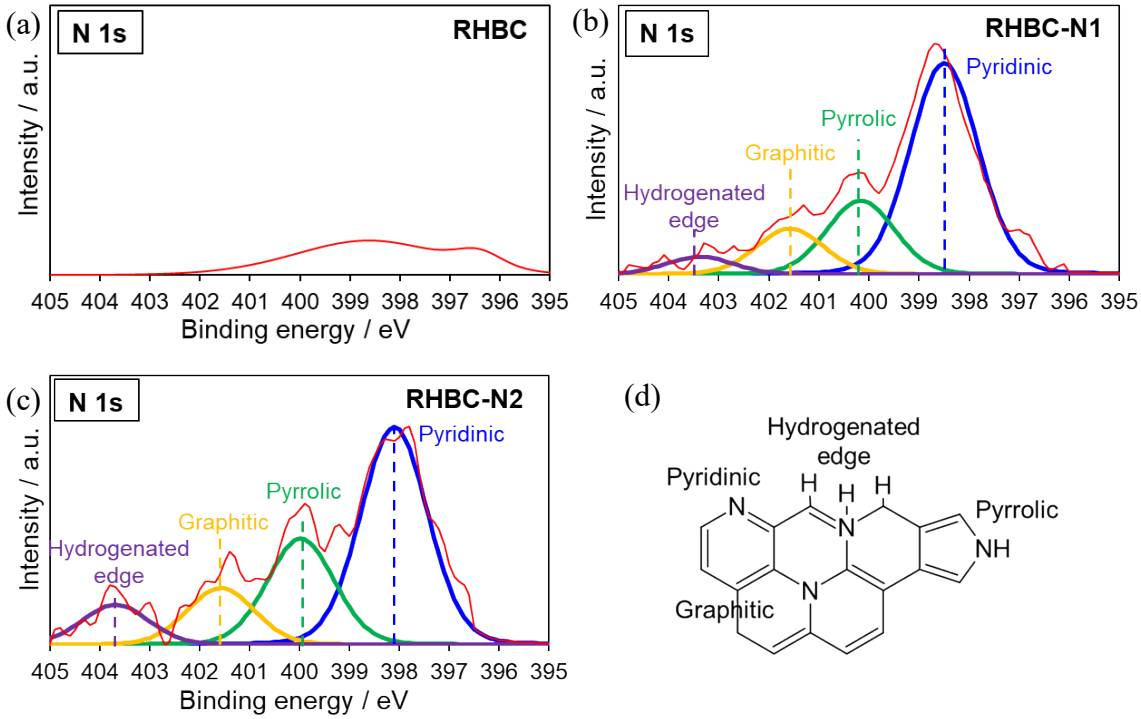

Figure 5. XPS N1s profiles for: (a) RHBC; (b) RHBC-N1; (c) RHBC-N2; and (d) schematic of the main detected nitrogen species.

3.2. DFT calculations

The sulfur adsorption process (i.e. H_2S removal from a gas stream) can be described by reactions (1) and (2). A higher concentration of O* on the surface of carbon is expected to assist the reaction. It has been shown in this study that when nitrogen is doped into the carbon phase of biochar, pyridinic-N, pyrrolic-N, and graphitic-N were produced. Among these, it has been reported that pyridinic-N promotes the formation of O* which can contribute to the promotion of oxygen reduction reaction (ORR) on the Pt-based electrocatalysts of fuel cells. As for the nitrogen-doped biochar, however, the H_2S adsorption mechanism is still not fully understood [21,47]. O_2 in a gas stream is considered to be an origin of O* even for a fuel stream. O_2 adsorption on graphene type structures has been reported [35]. For the formation of O*, the O-O bond needs to be broken, which is achieved by donating two more electrons to the degenerate π-molecular orbital in the oxygen molecule [48]. Pyridinic-N in the graphene structure has two unpaired electrons in the sp^2 hybridization orbitals, which could contribute to the dissociation of the O-O bond of the approached O_2 [49,50].To prove this phenomenon, the following DFT simulations were performed.

TABLE II. Interaction energy (E_{int}) between O_2 and N-doped graphene structure estimated by DFT.

		Energy / eV			**Interaction energy / eV**	**Distance of O-O bond / Å**
	Initial position of O_2	O_2 on graphene structure	O_2 only	Graphene structure		
Pyridinic–N	C adjacent to doped-N	-258.58	-9.85	-248.02	-0.71	1.23
	Doped-N	-260.98	-9.85	-248.02	-3.12	Broken
Pyrrolic–N	C adjacent to doped-N	-279.47	-9.85	-267.63	-2.00	1.44
	Doped-N	-279.47	-9.85	-267.63	-2.00	1.57
Graphitic-N	C adjacent to doped-N	-292.18	-9.85	-280.89	-1.45	1.32
	Doped-N	-292.21	-9.85	-280.89	-1.48	1.28

After the simulated graphene structures with pyridinic-, pyrrolic-, and graphitic-N moieties were optimized for the respective N-doped structures, an O_2 molecule was placed on the doped-N site or on the carbon adjacent to the doped-N site to compare their final configurations. The negative interaction energies shown in Table II indicate that O_2 can adsorb on the graphene structure for all cases. O_2 tended to adsorb more readily on the doped-N sites than on the adjacent carbon atom. The stability of the O_2 adsorbed on these nitrogen-doped graphene structures was in the order of graphitic-N < pyrrolic-N < pyridinic-N. As shown in Fig. 6, except for on pyridinic-N sites, the O_2 molecule remained near its initial position without decomposition. However, if the O_2 molecule was placed on the pyridinic-N site it decomposed, and the resulting oxygen atoms were adsorbed onto the carbon atoms in the pyridinic chain, as shown in Fig. 6a. This result indicates that two electrons (i.e. a lone pair) from the pyridinic-N site were supplied to the O_2 molecule, and that the O-O bond was stretched and finally broken, as the origin of the O* species.

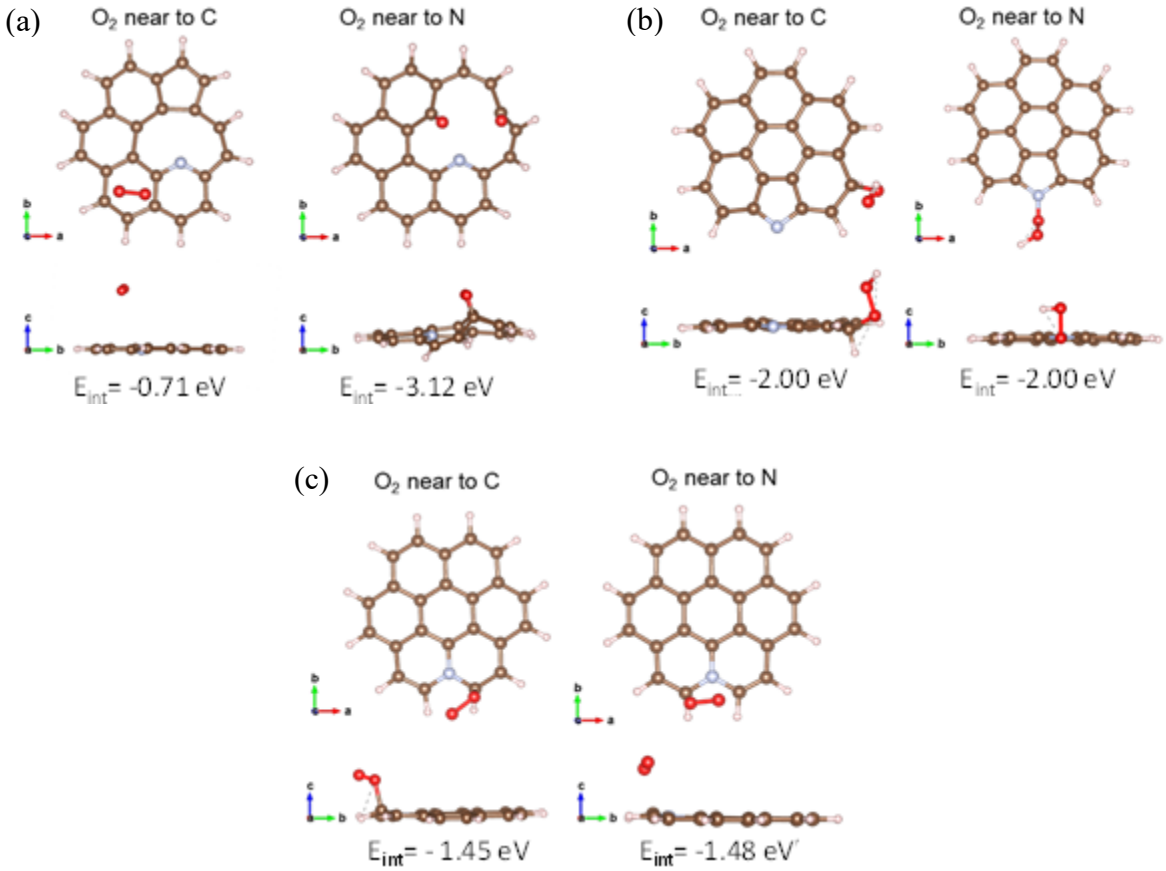

Figure 6. Optimized configurations for the adsorption of O_2 on (a) pyridinic-, (b) pyrrolic-, and (c) graphitic-N.

3.3. H_2S adsorption on powdered biochar

The H_2S adsorption results for the powdered biochar samples were measured at the gas hourly space velocity (GHSV) of 1,579 hr^{-1}, as shown in Fig. 7. The breakthrough capacity (q_0) and the total adsorption capacities (q) calculated from the breakthrough curve and using Equation (3) are summarized in Table III

As-prepared RHBC with the smallest SSA and without N doping had the lowest breakthrough capacity. RHBC-N1 has the largest breakthrough capacity, attributed to this sample having the highest pyridinic-N content (Table I), resulting in enhanced affinity with H_2S, as confirmed by the DFT calculations in the previous section. Due to this high affinity combined with large SSA, the rate of reaction (2) is relatively fast. q_0 of RHBC-N2 was only half of RHBC-N1 because of the lower content of pyridinic-N on the surface (0.75-fold of RHBC-N1) as well as half SSA (Table III).

Meanwhile, q of as-prepared RHBC is again the lowest of all the biochar samples. The value for RHBC-N1 is about 4 times larger, again attributed to the existence of pyridinic-N sites and the enhanced porosity (Table I). However, in this case, q of RHBC-N2 is the highest despite having lower nitrogen content and lower porosity. The reasons for this are elaborated upon in the following paragraphs.

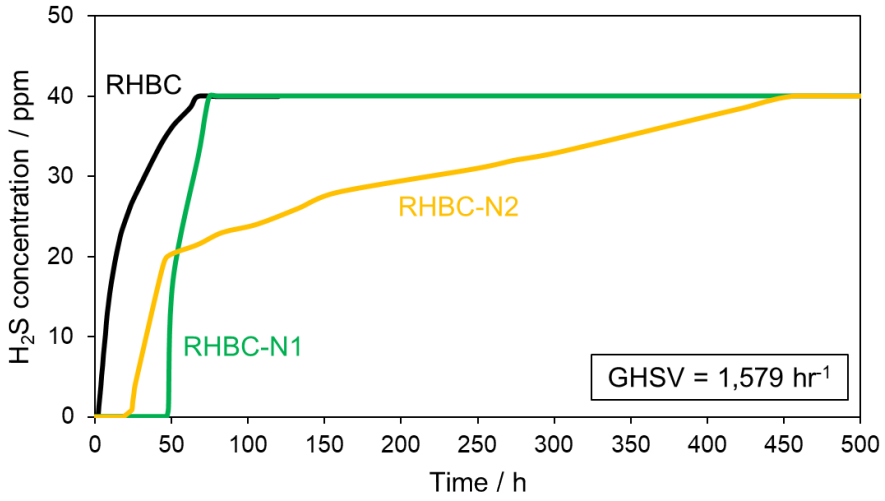

Figure 7. Results of H_2S adsorption tests for powdered rice husk biochar samples.

TABLE III. Breakthrough H_2S adsorption capacity (q_0) and total H_2S adsorption capacity (q) of the powdered and paper-structured rice husk biochar samples.

Sample		q_0 / mg.g^{-1}	q / mg.g^{-1}
Powdered	RHBC	0.27	2.54
	RHBC-N1	8.02	9.58
	RHBC-N2	3.96	23.0
Paper-structured	PS[RHBC]	1.30	14.7
	PS[RHBC-N2]	8.71	96.1

To gain more insight into the adsorption mechanism, and the differences in capacity between the samples, XPS S 2p profiles were measured on RHBC-N1 and RHBC-N2, after H_2S adsorption tests (Fig. 8).

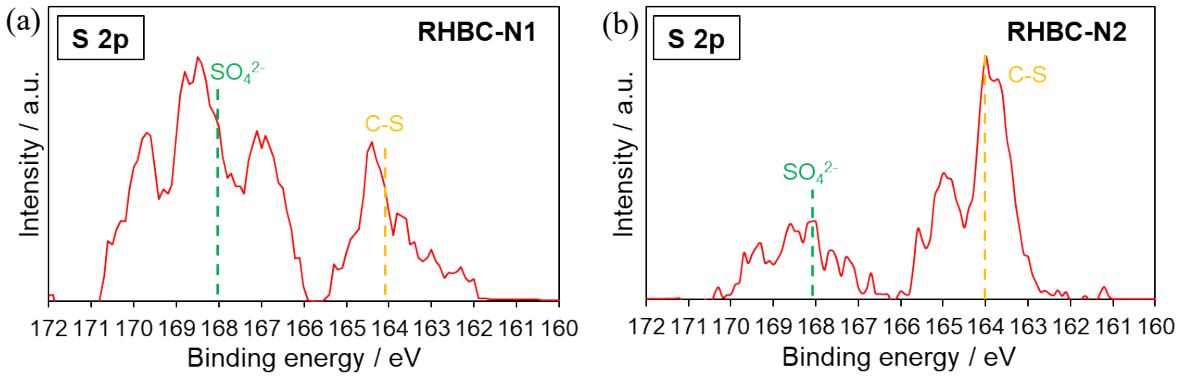

Figure 8. XPS profiles for S 2p after the H_2S adsorption tests (see Fig. 7); (a) RHBC-N1 and (b) RHBC-N2.

In the case of RHBC-N1, a relatively high proportion of sulfate species (~168 eV) is observed compared to sulfur species (~164 eV) [51,52]. The presence of sulfates is attributed to the high proportion of pyridinic-N and the associated O* species which can oxidize HS^- to form sulfate as follows:

$$HS^- + 4O^* \rightarrow SO_3 + OH^- \quad (5)$$
$$H^+ + OH^- \rightarrow H_2O \quad (6)$$
$$SO_3 + 3H_2O \rightarrow 2H_3O^+ + SO_4^{2-} \quad (7)$$

Meanwhile, for RHBC-N2, a higher proportion of C–S bonds (~164 eV) is observed [53] compared to sulfate species (~168 eV). This is attributed to the lower proportion of pyridinic-N and the associated O* species, suppressing sulfate formation.

SSA, pore volume and near-surface sulfur (S) contents after the H_2S adsorption test are summarized in Table IV. The near-surface S content after H_2S adsorption measured in the vacuum condition of XPS indicates the retainability of sulfur species. S could not be detected on the surface of the spent RHBC. The near-surface S content of the spent RHBC-N1 was only 1/7 of the spent RHBC-N2, even though the *q* of it was about half of RHBC-N2, indicating that S species adsorbed on the surface of RHBC-N1 is more easily detached from the surface under the vacuum condition compared to RHBC-N2.

TABLE IV. Results of the BET measurement and the XPS quantification of near-surface S content for the RHBC samples after the H_2S adsorption test.

Sample	SSA / m^2 g^{-1}	V_{tot} / 10^{-7} m^3 g^{-1}	ΔV_{tot} / 10^{-7} m^3 g^{-1}	V_{mic} / 10^{-7} m^3 g^{-1}	ΔV_{mic} / 10^{-7} m^3 g^{-1}	Near-surface S / wt%
RHBC	11.3	0.27	0.75	0.01	0.62	-
RHBC-N1	270	1.44	0.34	1.11	0.32	0.37
RHBC-N2	16.1	0.33	0.69	0.01	0.67	2.51

The pore size distributions of RHBC, RHBC-N1 and RHBC-N2 before and after H_2S adsorption tests are shown in Fig. 9. Before the adsorption test, RHBC-N1 has the highest proportion of micropores. After the H_2S adsorption test, there is only a small decrease in the fraction of accessible micropores. This indicates that the utilization rate of micropores in this sample for H_2S adsorption is relatively low. From the comparison between the values listed in Tables I and IV, it is clear that RHBC and RHBC-N2 lost almost all micropore volume after H_2S adsorption, whereas RHBC-N1 lost only around 20%, indicating that the adsorbed sulfur did not well penetrate into the micropores of RHBC-N1. As shown in Fig. 8, the dominant sulfur species on the spent RHBC-N1 was sulfate resulting from the higher content of O*. The low retainability of sulfur species of RHBC-N1 under the vacuum condition is probably derived from the sulfate species existing outside the micropores.

However, in the case of RHBC-N2, before the H_2S adsorption test, the proportion of micropores is lower than for RHBC-N1, as reflected in the lower surface area and pore volume (Table I). After the H_2S adsorption test, the proportion of micropores in RHBC-N2 is dramatically decreased. Even under the vacuum condition, the adsorbed sulfur (C-S) does not easily desorb. This suggests that the micropores are almost completely filled with adsorbed sulfur species, corresponding to high micropore utilization rate, and providing an explanation for the higher measured total adsorption capacity despite the lower SSA and pore volume.

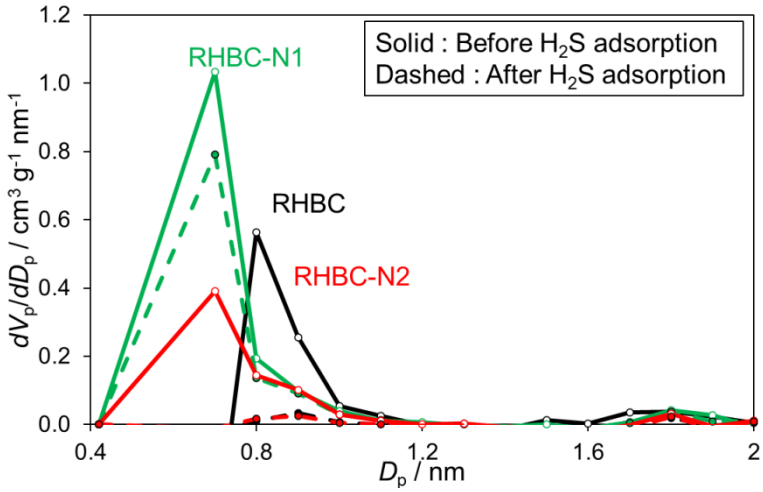

Figure 9. Pore size distributions of RHBC, RHBC-N1 and RHBC-N2 before and after H_2S adsorption tests (see Fig. 7), obtained from nitrogen adsorption/desorption isotherms using the MP method. V_p is the pore volume and D_p is the pore diameter.

The proposed reason for the difference in adsorption behavior between RHBC-N1 and RHBC-N2 is described schematically in Fig. 10. For RHBC-N1, the higher abundance pyridinic-N sites result in a high proportion of O* species on the surface (as confirmed by XPS). These promote the formation of sulfur via H_2S adsorption. However, we propose that the formation rate of sulfur is higher than the diffusion rate into the micropores, resulting in an accumulation of sulfur on the surface. This accumulated sulfur is then further oxidized to form sulfate, as observed by XPS after adsorption tests. This sulfate prevents subsequent diffusion of sulfur into the micropores, limiting the total H_2S adsorption capacity. This is consistent with the fact that this sample has the highest breakthrough capacity, but low total adsorption capacity. In short, the micropores are not well utilized as adsorption sites in this case.

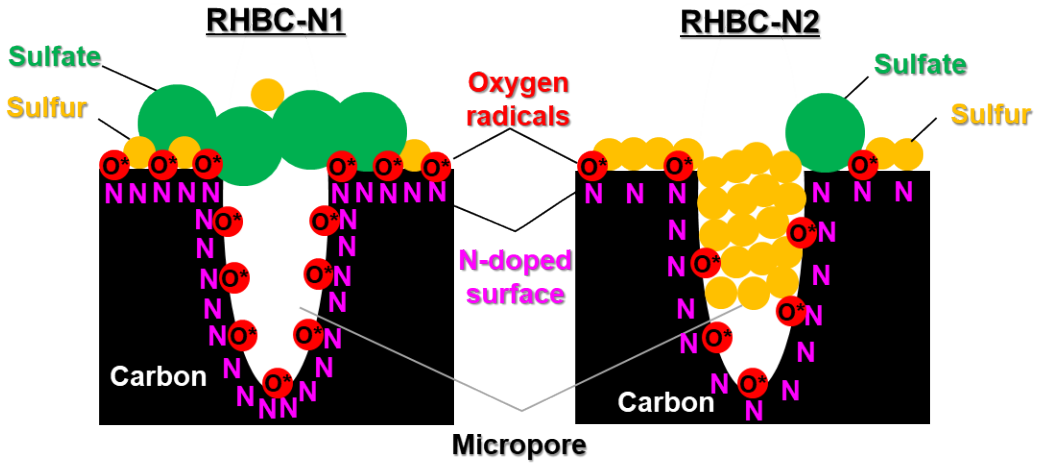

Figure 10. Schematic illustration explaining the difference in H_2S adsorption behavior between RHBC-N1 and RHBC-N2.

On the other hand, the total adsorption capacity of RHBC-N2 is double that of RHBC-N1, despite the lower nitrogen content. In this case, we propose that lower nitrogen content leads to a lower abundance of O* species on the surface. This keeps the sulfur formation

rate below the diffusion rate, meaning that diffusion of sulfur into the micropores can occur unhindered by sulfate formation. This is confirmed by the low sulfate content observed by XPS and the low micropore volume after H_2S adsorption tests. This is consistent with the low breakthrough capacity and the high total H_2S adsorption capacity.

3.5. Viability of Nitrogen-doped Biochar as a Desulfurizer for SOFCs

The nitrogen-doped biochar developed in this study is intended to be used for the second step of biogas desulfurization before being supplied to an SOFC. Using the results obtained above, the mass (M_{BC}) of biochar required for 100,000 h operation for a 1 kW SOFC was estimated using the following equation:

$$Desulfurizer\ lifetime = \frac{q\, M_{BC}}{V_{biogas}\, C_{H2S}\, \rho_{H2S}} \quad (8)$$

where V_{biogas} is the flow rate of the biogas; C_{H2S} is the concentration of H_2S in the biogas; and ρ_{H2S} is the density of H_2S, 1.36 kg Nm^{-3}.

In a biogas-fueled SOFC demonstration reported by Shiratori *et al.* [25], biogas passed through a desulfurizing tower packed with 40 kg of iron oxide pellets, resulting in a concentration of C_{H2S} = 4 ppm. This was supplied at V_{biogas} = 0.33 $Nm^3\ h^{-1}$ to the SOFC system resulting in 1 kW of power generation. For continuous supply of H_2S-free biogas to the SOFC, the breakthrough capacity (q_o = 3.96 $mg.g^{-1}$) can be used, corresponding to a mass of 45 kg. If the adsorption capacity of powdered biochar RHBC-N2 is fully utilized (q = 23.0 $mg.g^{-1}$), the required mass can be decreased to 7.8 kg. These estimations indicate the clear viability of using nitrogen-doped biochar as a desulfurizer for biogas-fueled SOFC systems, as well as the feasibility of using digestate liquid as an alternative source of NH_3.

Conclusions

Biochar was prepared by the pyrolysis of rice husk for utilization as a sustainable H_2S adsorbent for biogas-fueled SOFCs. The effect of nitrogen-doping was investigated via high temperature NH_3 treatment using different methods. Using pure NH_3 gas is not always feasible in rural locations, so digestate liquid containing ammonium ions was considered as an alternative. As such, rice husk biochar samples were doped with nitrogen either using NH_3 gas from a cylinder, or by bubbling carrier gas through an aqueous NH_3 solution.

Nitrogen-doping was confirmed to be effective in increasing the total H_2S adsorption capacity. This was attributed to the formation of pyridinic-N sites, and their affinity with O* species which can catalyze the conversion of hydrogen sulfide to sulfur. Counterintuitively, higher nitrogen-doping levels resulted in lower adsorption capacity. This was attributed to the promotion of sulfate formation, resulting in a lower micropore utilization rate.

The nitrogen-doped biochar was assessed as the secondary desulfurizer for supplying biogas to a SOFC. It was calculated that, for the biogas containing 4 ppm H_2S, just 45 kg of nitrogen-doped biochar would be required to supply H_2S-free biogas for 100,000 h operation of 1 kW SOFC. Biochar doped with nitrogen using the digestate liquid is a promising material as desulfurizer.

Acknowledgements

This work was supported by JSPS KAKENHI, Fostering Joint International Research (B), Grant Number 20KK0248.

References

[1] Y. Shiratori, T. Quang-Tuyen, K. Sasaki, Performance enhancement of biodiesel fueled SOFC using paper-structured catalyst, Int. J. Hydrogen Energy. 38 (2013) 9856–9866. https://doi.org/10.1016/j.ijhydene.2013.05.128.

[2] Y. Gao, J. Jiang, Y. Meng, F. Yan, A. Aihemaiti, A review of recent developments in hydrogen production via biogas dry reforming, Energy Convers. Manag. 171 (2018) 133–155. https://doi.org/10.1016/j.enconman.2018.05.083.

[3] A.G. Skerman, S. Heubeck, D.J. Batstone, S. Tait, Low-cost filter media for removal of hydrogen sulphide from piggery biogas, Process Saf. Environ. Prot. 105 (2017) 117–126. https://doi.org/10.1016/j.psep.2016.11.001.

[4] H. Setiawan, T.-G. Yu, T.G.H. Nguyen, M. Sakamoto, T. Uchida, Y. Shiratori, Fuel impurity poisoning of Ru/γ-Al_2O_3 catalyst packed in the reformer for biogas-fueled SOFC system , ECS Trans. 91 (2019) 1651–1659. https://doi.org/10.1149/09101.1651ecst.

[5] K. Haga, S. Adachi, Y. Shiratori, K. Itoh, K. Sasaki, Poisoning of SOFC anodes by various fuel impurities, Solid State Ionics. 179 (2008) 1427–1431. https://doi.org/10.1016/j.ssi.2008.02.062.

[6] K. Sasaki, K. Susuki, A. Iyoshi, M. Uchimura, N. Imamura, H. Kusaba, Y. Teraoka, H. Fuchino, K. Tsujimoto, Y. Uchida, N. Jingo, H_2S poisoning of solid oxide fuel cells, J. Electrochem. Soc. 153 (2006) A2023. https://doi.org/10.1149/1.2336075.

[7] A.G. Georgiadis, N.D. Charisiou, M.A. Goula, Removal of hydrogen sulfide from various industrial gases: A review of the most promising adsorbing materials, Catalysts. 10 (2020) 521. https://doi.org/10.3390/catal10050521.

[8] S.P. Sohi, E. Krull, E. Lopez-Capel, R. Bol, A review of biochar and its use and function in soil, Adv. Agron. 105 (2010) 47–82. https://doi.org/10.1016/S0065-2113(10)05002-9.

[9] D. Savova, E. Apak, E. Ekinci, F. Yardim, N. Petrov, T. Budinova, M. Razvigorova, V. Minkova, Biomass conversion to carbon adsorbents and gas, Biomass and Bioenergy. 21 (2001) 133–142. https://doi.org/10.1016/S0961-9534(01)00027-7.

[10] M. Waqas, A.S. Aburiazaiza, R. Miandad, M. Rehan, M.A. Barakat, A.S. Nizami, Development of biochar as fuel and catalyst in energy recovery technologies, J. Clean. Prod. 188 (2018) 477–488. https://doi.org/10.1016/j.jclepro.2018.04.017.

[11] Z. Liu, A. Quek, S. Kent Hoekman, R. Balasubramanian, Production of solid biochar fuel from waste biomass by hydrothermal carbonization, Fuel. 103 (2013) 943–949. https://doi.org/10.1016/j.fuel.2012.07.069.

[12] W. Suliman, J.B. Harsh, N.I. Abu-Lail, A.M. Fortuna, I. Dallmeyer, M. Garcia-Pérez, The role of biochar porosity and surface functionality in augmenting hydrologic properties of a sandy soil, Sci. Total Environ. 574 (2017) 139–147. https://doi.org/10.1016/j.scitotenv.2016.09.025.

[13] H.M. El Sharkawi, S. Tojo, T. Chosa, F.M. Malhat, A.M. Youssef, Biochar-ammonium phosphate as an uncoated-slow release fertilizer in sandy soil, Biomass and Bioenergy. 117 (2018) 154–160. https://doi.org/10.1016/j.biombioe.2018.07.007.

[14] Y. Zhu, W. Tang, X. Jin, B. Shan, Using biochar capping to reduce nitrogen release from sediments in eutrophic lakes, Sci. Total Environ. 646 (2019) 93–104. https://doi.org/10.1016/j.scitotenv.2018.07.277.

[15] H. Bamdad, K. Hawboldt, S. MacQuarrie, A review on common adsorbents for acid gases removal: Focus on biochar, Renew. Sustain. Energy Rev. 81 (2018) 1705–1720. https://doi.org/10.1016/j.rser.2017.05.261.

[16] M.I. Inyang, B. Gao, Y. Yao, Y. Xue, A. Zimmerman, A. Mosa, P. Pullammanappallil, Y.S. Ok, X. Cao, A review of biochar as a low-cost adsorbent for aqueous heavy metal removal, Crit. Rev. Environ. Sci. Technol. 46 (2016) 406–433. https://doi.org/10.1080/10643389.2015.1096880.

[17] B. Sajjadi, W.Y. Chen, N.O. Egiebor, A comprehensive review on chemical activation of biochar for energy and environmental applications, Rev. Chem. Eng. 35 (2018) 735–776. https://doi.org/10.1515/revce-2018-0003.

[18] I. Isik-Gulsac, Investigation of impregnated activated carbon properties used in hydrogen sulfide fine removal, Brazilian J. Chem. Eng. 33 (2016) 1021–1030. https://doi.org/10.1590/0104-6632.20160334s20150164.

[19] X. Yang, S. Zhang, M. Ju, L. Liu, Preparation and modification of biochar materials and their application in soil remediation, Appl. Sci. 9 (2019) 1365. https://doi.org/10.3390/app9071365.

[20] D. Li, W. Chen, J. Wu, C.Q. Jia, X. Jiang, Preparation of waste biomass-derived N-doped carbons and the application in acid gases removal: Focus on N functional groups, J. Mater. Chem. A. 8 (2020) 24977–24995. https://doi.org/10.1039/d0ta07977d.

[21] S. Li, Q. Gu, N. Cao, Q. Jiang, C. Xu, C. Jiang, C. Chen, C. Pham-Huu, Y. Liu, Defect enriched N-doped carbon nanoflakes as robust carbocatalysts for H_2S selective oxidation, J. Mater. Chem. A. 8 (2020) 8763–9400. https://doi.org/10.1039/d0ta00212g.

[22] W. Shen, W. Fan, Nitrogen-containing porous carbons: Synthesis and application, J. Mater. Chem. A. 1 (2013) 999–1013. https://doi.org/10.1039/c2ta00028h.

[23] Y. Shiratori, T. Yamakawa, M. Sakamoto, H. Yoshida, T. Kitaoka, Q.T. Tran, D.C.T. Doan, M.C. Dang, Biogas production from local biomass feedstock in the Mekong delta and its utilization for a direct internal reforming solid oxide fuel cell, Front. Environ. Sci. 5 (2017) 25. https://doi.org/10.3389/fenvs.2017.00025.

[24] M. Baldi, M.C. Collivignarelli, A. Abbà, I. Benigna, The valorization of ammonia in manure digestate by means of alternative stripping reactors, Sustain. 10 (2018) 3073. https://doi.org/10.3390/su10093073.

[25] Y. Shiratori, M. Sakamoto, T.G.H. Nguyen, T. Yamakawa, T. Kitaoka, H. Matsubara, Y. Watanabe, S. Nakatsuka, T.C.D. Doan, C.M. Dang, Biogas power generation with SOFC to demonstrate energy circulation suitable for Mekong delta, Vietnam, Fuel Cells. 19 (2019) 346–353. https://doi.org/10.1002/fuce.201800184.

[26] G. Kresse, J. Furthmüller, Efficiency of ab-initio total energy calculations for metals and semiconductors using a plane-wave basis set, Comput. Mater. Sci. 6 (1996) 15–50. https://doi.org/10.1016/0927-0256(96)00008-0.

[27] G. Kresse, D. Joubert, From ultrasoft pseudopotentials to the projector augmented-wave method, Phys. Rev. B - Condens. Matter Mater. Phys. 59 (1999) 1758–1775. https://doi.org/10.1103/PhysRevB.59.1758.

[28] G. Kresse, J. Furthmuller, Efficient iterative schemes for ab initio total-energy calculations using a plane-wave basis set, Phys. Rev. B. 54 (1996) 11169–11186. https://doi.org/10.1103/physrevb.54.11169.

[29] J.P. Perdew, K. Burke, M. Ernzerhof, Generalized gradient approximation made simple, Phys. Rev. Lett. 77 (1996) 3865–3868. https://doi.org/10.1103/PhysRevLett.77.3865.

[30] Q. Ren, N. Qin, B. Liu, Y. Yao, X. Zhao, Z. Deng, Y. Li, Y. Dong, D. Qian, B.L. Su, W. Zhang, H.E. Wang, An oxygen-deficient vanadium oxide@N-doped carbon heterostructure for sodium-ion batteries: Insights into the charge storage mechanism and enhanced reaction kinetics, J. Mater. Chem. A. 8 (2020) 3450–3458. https://doi.org/10.1039/c9ta11965e.

[31] P.R. Wallace, The band theory of graphite, Phys. Rev. 71 (1947) 622–634. https://doi.org/10.1103/PhysRev.71.622.

[32] H. Gao, Z. Liu, DFT study of NO adsorption on pristine graphene, RSC Adv. 7 (2017) 13082–13091. https://doi.org/10.1039/c6ra27137e.

[33] E. V. Castro, K.S. Novoselov, S. V. Morozov, N.M.R. Peres, J.M.B. Lopes Dos Santos, J. Nilsson, F. Guinea, A.K. Geim, A.H. Castro Neto, Electronic properties of a biased graphene bilayer, J. Phys. Condens. Matter. 22 (2010). https://doi.org/10.1088/0953-8984/22/17/175503.

[34] T. Bučko, S. Lebègue, J. Hafner, J.G. Ángyán, Tkatchenko-Scheffler van der Waals correction method with and without self-consistent screening applied to solids, Phys. Rev. B - Condens. Matter Mater. Phys. 87 (2013) 1–15. https://doi.org/10.1103/PhysRevB.87.064110.

[35] A.S. Dobrota, I.A. Pašti, S. V. Mentus, N. V. Skorodumova, A DFT study of the interplay between dopants and oxygen functional groups over the graphene basal plane - Implications in energy-related applications, Phys. Chem. Chem. Phys. 19 (2017) 8530–8540. https://doi.org/10.1039/c7cp00344g.

[36] M. Stöhr, R. Podloucky, S. Müller, Ab initio phase diagram of oxygen adsorption on W(110), J. Phys. Condens. Matter. 21 (2009). https://doi.org/10.1088/0953-8984/21/13/134017.

[37] H. Setiawan, M. Sakamoto, Y. Shiratori, T. Fujisaki, N-doped biochar as H_2S adsorbent for the biogas-fueled SOFC, ECS Meet. Abstr. MA2021-03 (2021) 79–79. https://doi.org/10.1149/ma2021-03179mtgabs.

[38] H. Setiawan, M. Sakamoto, Y. Shiratori, Study on biochar as desulfurizer for SOFC application, Fuel Cells. 21 (2021) 430–439. https://doi.org/10.1002/fuce.202100025.

[39] L. Zhou, P. Chen, M. Li, Y. Zhou, A study of the removal of minor amounts of H2S from natural gas by activated carbon, Adsorpt. Sci. Technol. 20 (2002) 969–976. https://doi.org/10.1260/026361702321705258.

[40] Xylem vessel definition and examples - Biology Online Dictionary, https://www.biologyonline.com/dictionary/xylem-vessel (accessed January 11, 2022).

[41] W. Suliman, J.B. Harsh, N.I. Abu-Lail, A.M. Fortuna, I. Dallmeyer, M. Garcia-Perez, Influence of feedstock source and pyrolysis temperature on biochar bulk and surface properties, Biomass and Bioenergy. 84 (2016) 37–48. https://doi.org/10.1016/j.biombioe.2015.11.010.

[42] K.P. Gadkaree, Carbon honeycomb structures for adsorption applications, Carbon N. Y. 36 (1998) 981–989. https://doi.org/10.1016/S0008-6223(97)00230-3.

[43] M.S. Shafeeyan, W.M.A.W. Daud, A. Houshmand, A. Shamiri, A review on surface modification of activated carbon for carbon dioxide adsorption, J. Anal. Appl. Pyrolysis. 89 (2010) 143–151. https://doi.org/10.1016/j.jaap.2010.07.006.

[44] I. Bertóti, M. Mohai, K. László, Surface modification of graphene and graphite by nitrogen plasma: Determination of chemical state alterations and assignments by quantitative X-ray photoelectron spectroscopy, Carbon N. Y. 84 (2015) 185–196. https://doi.org/10.1016/j.carbon.2014.11.056.

[45] L. Xiong, X.F. Wang, L. Li, L. Jin, Y.G. Zhang, S.L. Song, R.P. Liu, Nitrogen-enriched porous carbon fiber as a CO_2 adsorbent with superior CO_2 selectivity by air activation, Energy and Fuels. 33 (2019) 12558–12567. https://doi.org/10.1021/acs.energyfuels.9b02769.

[46] L. Leng, S. Xu, R. Liu, T. Yu, X. Zhuo, S. Leng, Q. Xiong, H. Huang, Nitrogen containing functional groups of biochar: An overview, Bioresour. Technol. (2019) 122286. https://doi.org/10.1016/j.biortech.2019.122286.

[47] Q. Wu, Y. Xian, Z. He, Q. Zhang, J. Wu, G. Yang, X. Zhang, H. Qi, J. Ma, Y. Xiao, L. Long, Adsorption characteristics of Pb(II) using biochar derived from spent mushroom substrate, Sci. Rep. 9 (2019) 1–11. https://doi.org/10.1038/s41598-019-52554-2.

[48] F. Hess, A.T. Staykov, B. Yildiz, J. Kilner, Solid oxide fuel cell materials and interfaces, in: W. Andreoni, S. Yip (Eds.), Handb. Mater. Model. Appl. Curr. Emerg. Mater., Second, Springer Nature Switzerland AG 2020, Cham, 2020: pp. 1275–1305. https://doi.org/10.1007/978-3-319-44680-6_132.

[49] M. Kunaseth, P. Poldorn, A. Junkeaw, J. Meeprasert, C. Rungnim, S. Namuangruk, N. Kungwan, C. Inntam, S. Jungsuttiwong, A DFT study of volatile organic compounds adsorption on transition metal deposited graphene, Appl. Surf. Sci. 396 (2017) 1712–1718. https://doi.org/10.1016/j.apsusc.2016.11.238.

[50] C.P. Ewels, M. Glerup, Nitrogen doping in carbon nanotubes, J. Nanosci. Nanotechnol. 5 (2005) 1345–1363. https://doi.org/10.1166/jnn.2005.304.

[51] K.S. Siow, L. Britcher, S. Kumar, H.J. Griesser, XPS study of sulfur and phosphorus compounds with different oxidation states, Sains Malaysiana. 47 (2018) 1913–1922. https://doi.org/10.17576/jsm-2018-4708-33.

[52] D.C. Frost, W.R. Leeder, R.L. Tapping, X-ray photoelectron spectroscopic investigation of coal, Fuel. 53 (1974) 206–211. https://doi.org/10.1016/0016-2361(74)90013-1.

[53] L. Zhao, G. Liu, P. Zhang, L. Sun, L. Cong, T. Wu, B. Zhang, W. Lu, H. Xie, H. Wang, Nitrogen-sulfur dual-doped porous carbon spheres/sulfur composites for high-performance lithium-sulfur batteries, RSC Adv. 9 (2019) 16571–16577. https://doi.org/10.1039/c9ra00768g.